Check for updates

How to cite: *Angew. Chem. Int. Ed.* **2025**, *64*, e202501190
doi.org/10.1002/anie.202501190

Ammonia Synthesis | **Very Important Paper**

Single-Atom Fe Catalysts With Improved Metal Loading for Efficient Ammonia Synthesis Under Mild Conditions

Yuting Jiang, Ziquan Chen, Tao Peng, Long Jiao, Xiulian Pan, Hai-Long Jiang, and Xinhe Bao**

Abstract: Ammonia synthesis is a cornerstone in the chemical industry. Given that the traditional Haber–Bosch (H-B) process requires very high temperature and pressure, it is imperative to develop catalysts capable of facilitating ammonia synthesis under mild conditions. In this work, a post-metal replacement strategy is developed to improve the Fe loading in single-atom Fe-implanted N-doped carbon catalysts. Starting from the Zn–Fe–N–C material with single-atom Zn and Fe sites coexisting in N-doped porous carbon pyrolyzed from porphyrinic metal–organic frameworks (MOFs), the replacement of single-atom Zn with Fe sites is performed, which significantly increases the Fe loading from 1.33 to 2.39 wt%. This effectively suppresses the migration and agglomeration of Fe, yielding Fe–N–C with high metal loading (Fe_{HL}–N–C). Notably, the Fe_{HL}–N–C catalyst exhibits a catalytic rate of 558 $\mu mol \cdot g_{cat}^{-1} \cdot h^{-1}$ at 300 °C for ammonia synthesis at atmospheric pressure, far surpassing the performance of the traditional dominant fused iron and even Ru-based precious metal catalysts.

Introduction

Ammonia, as a crucial inorganic compound, plays significant roles in diverse industrial sectors encompassing fertilizer and pharmaceutical production.[1–6] With notably high hydrogen content (17.7 wt%) and substantial energy density (3.5 kW $h \cdot kg^{-1}$), ammonia is a highly storable and transportable substance that can serve as a contender for a carbon-free energy vector.[7,8] Although the synthesis of ammonia from nitrogen (N_2) holds paramount significance for human civilization, the energy-intensive Haber–Bosch process, operated under high temperatures and pressures, is still the predominant industrial-scale ammonia production route, resulting in 2% of global energy consumption and 1.4% of global CO_2 emissions.[9–11] Implementing ammonia synthesis under mild conditions remains a great challenge, and the development of cost-effective catalysts that can produce ammonia efficiently is highly desired.[12–14]

Traditionally, iron (Fe) or ruthenium (Ru)-based catalysts are the most commonly used for ammonia synthesis in industry. However, this process requires substantial energy input to dissociate molecular N_2 due to the extraordinarily stable triple bond (945 $kJ \cdot mol^{-1}$).[15–17] To enhance the catalytic production of NH_3 under mild conditions, the performance of Fe and Ru-based catalysts requires additional optimization and improvement. Previous investigations indicate that ammonia synthesis is sensitive to catalyst structure, and even minor structural modifications can result in significant changes in catalytic activity.[18,19] Therefore, precise fabrication of catalysts at the atomic scale is crucial for achieving optimal catalytic performance. Single-atom catalysts (SACs), characterized by atomically dispersed metal centers, ensure uniformity of the catalytic metal sites and enable precise design and regulation of their coordination environments.[20–25] This offers significant opportunities for the development of highly efficient catalysts toward catalyzing NH_3 synthesis under mild conditions.[26–31] However, due to the high surface energy, single-atom sites are prone to sintering during preparation or catalytic reactions; to avoid this, low metal loading in SACs is typically required.[32–34] Establishing a construction methodology for stable SACs, particularly with high metal loadings, is highly desirable yet remains a significant challenge.

Metal–organic frameworks (MOFs),[35–39] featuring well-defined structures, high porosity, large surface area, easy tailorability, and adjustable chemical composition, have attracted extensive interest in heterogeneous catalysis.[40–43] In recent years, MOFs have been recognized as ideal precursors for accurately constructing SACs via pyrolysis.[44–52] The obtained SACs derived from MOFs largely inherit the precursors' high surface area and porous structure, facilitating the exposure of active sites and promoting efficient mass transfer during the catalytic process.[46,47] Consequently, MOFs exhibit substantial potential for the precise fabrication and performance enhancement of SACs for various catalytic

[*] Y. Jiang, T. Peng, L. Jiao, H.-L. Jiang, X. Bao
Hefei National Research Center for Physical Sciences at the Microscale, School of Chemistry and Materials Science, University of Science and Technology of China, Hefei, Anhui 230026, P.R. China
E-mail: jianglab@ustc.edu.cn
xhbao@dicp.ac.cn

Y. Jiang, Z. Chen, X. Pan, X. Bao
State Key Laboratory of Catalysis, Dalian National Laboratory for Clean Energy, 2011-Collaborative Innovation Center of Chemistry for Energy Materials, Dalian Institute of Chemical Physics, Chinese Academy of Sciences, Dalian, Liaoning 116023, P.R. China

Homepage: http://mof.ustc.edu.cn/

Additional supporting information can be found online in the Supporting Information section

© 2025 Wiley-VCH GmbH

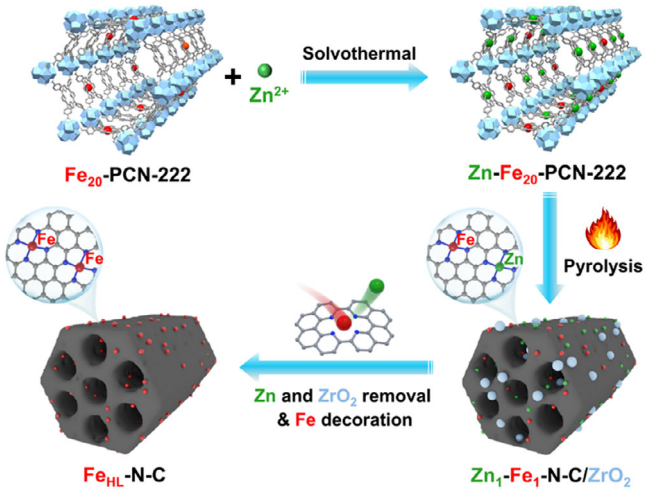

Scheme 1. Illustration of the synthetic route to the Fe_{HL}–N–C.

applications.[48–51] The prevailing synthetic strategy for MOF-based SACs relies on mixed metals, mixed linkers, and/or pore confinement to augment the distance between neighboring metal atoms, thereby preventing metal atom aggregation during pyrolysis.[44,46,49–51] Nevertheless, this approach yields SACs with relatively low metal loading, highlighting an urgent need to improve metal content in MOF-based SACs, which remains a critical challenge.

Inspired by the post-metallization strategy for constructing metal porphyrin complexes, the monatomic metal loading can be improved by introducing porphyrins with different metal centers and performing ion exchange following pyrolysis. Considering the above, a kind of porphyrinic MOF (Zn–Fe_{20}–PCN-222) with 20% Fe-TCPP and 80% Zn-TCPP (TCPP = tetrakis (4-carboxyphenyl) porphyrin) is chosen as the precursor and affords Zn_1–Fe_1–N–C/ZrO_2 composites with single-atom Zn and Fe sites implanted in N-doped carbon after pyrolysis (Scheme 1). Subsequently, both ZrO_2 and Zn atoms are removed by acid etching, creating numerous high-energy Zn vacancies that can be easily decorated with other metal atoms. When external Fe atoms are introduced by a post-metal replacement strategy, they can spontaneously occupy the Zn vacancies, forming additional single-atom Fe sites by Fe–N coordination to lower the system energy. In this way, the Fe_{HL}–N–C with increased single-atom Fe loading is elaborately fabricated. Notably, the Fe_{HL}–N–C catalyst efficiently catalyzes ammonia synthesis under mild conditions, exhibiting a catalytic rate of 558 $\mu mol \cdot g_{cat}^{-1} \cdot h^{-1}$ at 300 °C and 1 bar. However, the traditional industrial fused Fe catalyst and Co_3Mo_3N catalyst necessitate harsher conditions to achieve comparable ammonia production rates. For example, at 300 °C and 10 bar, their catalytic activities are measured to be 346 and 423 $\mu mol \cdot g_{cat}^{-1} \cdot h^{-1}$, respectively.[53]

Results and Discussion

A series of isostructural porphyrinic MOFs, denoted as Fe_x-PCN-222 (x%: mole percentage of Fe-TCPP in the total sum of Fe-TCPP and nonmetallic H_2-TCPP linkers, x = 10, 20, 40, and 80), have been successfully constructed using a previously reported mixed linker strategy (Figure S1).[50] Upon the pyrolysis of Fe_x–PCN–222 in N_2 atmosphere at 800 °C followed by the removal of ZrO_2, Fe_x–N–C (x = 10, 20, 40, and 80) can be successfully obtained. Powder X-ray diffraction (XRD) patterns of all Fe_x–N–C catalysts exhibit two broad peaks corresponding to the (002) and (101) planes of carbon, while no metallic phase is detected (Figure S2). This manifests that Fe species exist in the form of single atoms or small aggregates without the presence of large Fe particles. To confirm the existing form of Fe, X-ray absorption spectroscopy (XAS) analysis was performed, showing that no Fe–Fe bonding is detected in Fe_{10}–N–C and Fe_{20}–N–C, confirming the atomic dispersion of Fe (Figures S3 and S4), in accordance with the transmission electron microscope (TEM) observation (Figures S5 and S6). Unfortunately, the further addition of Fe-TCPP in Fe_x-PCN-222 (x = 40 and 80) results in the formation of Fe nanoparticles with average particle sizes of 10.9 and 35.7 nm in Fe_{40}–N–C and Fe_{80}–N–C, respectively (Figures S7 and S8). These findings support that Fe_{20}–N–C with the Fe loading of 1.33 wt% is a crucial threshold for forming single-atom Fe sites via direct pyrolysis of Fe_x-PCN-222, limiting the further increase of Fe loading (Table S1). Achieving atomic dispersion of metal sites at higher loadings remains a primary objective.

To achieve atomic dispersion of Fe at higher loadings, a post-metal replacement strategy has been developed with the assistance of Zn atoms to improve the Fe loading based on Fe_{20}-PCN-222 (the precursor with the highest Fe loading to obtain single-atom Fe by direct pyrolysis). Specifically, by incorporating Zn into the non-metalized H_2-TCPP linkers of Fe_{20}-PCN-222, then Zn–Fe_{20}–PCN-222 is synthesized with the vacant porphyrin centers in the parent Fe_{20}–PCN–222 occupied by Zn ions (Figure S9). Scanning electron microscopy (SEM) reveals the retained rod-like morphology of Zn–Fe_{20}–PCN-222 with an approximate diameter of 280 nm (Figure 1a). Ultraviolet–visible (UV–vis) spectroscopy illustrates that the porphyrins in Zn–Fe_{20}–PCN-222 exhibit a slight broadening and redshift of the Soret band compared to PCN-222 involving non-metalized H_2-TCPP linkers, along with the reduced number of Q bands to two, manifesting a more symmetrical molecular structure (Figure S10). This confirms the metallization of all porphyrins in Zn–Fe_{20}–PCN-222.[54] The Fe_{HL}–N–C can be obtained through two subsequent processing steps: 1) the pyrolysis of Zn–Fe_{20}–PCN-222 at 800 °C under N_2 atmosphere; 2) the acid etching of Zn–Fe_{20}–PCN-222 to remove Zn species and ZrO_2, followed by the decoration of external Fe atoms. SEM observation shows the rod-like morphology. Fe_{HL}–N–C similar to Zn–Fe_{20}–PCN-222, yet with a noticeable size shrinkage (Figure S11). The TEM image of Fe_{HL}–N–C reveals no discernible Fe nanoparticles (Figure 1b). To provide detailed evidence of the formation of single-atom Fe sites within Fe_{HL}–N–C, the aberration-corrected high-angle annular dark-field scanning transmission electron microscopy (HAADF-STEM) is employed, and the isolated bright spots confirm that the Fe atoms are atomically dispersed in Fe_{HL}–N–C (Figure 1c). Energy-dispersive spectroscopy (EDS)

© 2025 Wiley-VCH GmbH

15213773, 2025, 27, Downloaded from https://onlinelibrary.wiley.com/doi/10.1002/anie.202501190 by University Of Science, Wiley Online Library on [13/08/2025]. See the Terms and Conditions (https://onlinelibrary.wiley.com/terms-and-conditions) on Wiley Online Library for rules of use; OA articles are governed by the applicable Creative Commons License

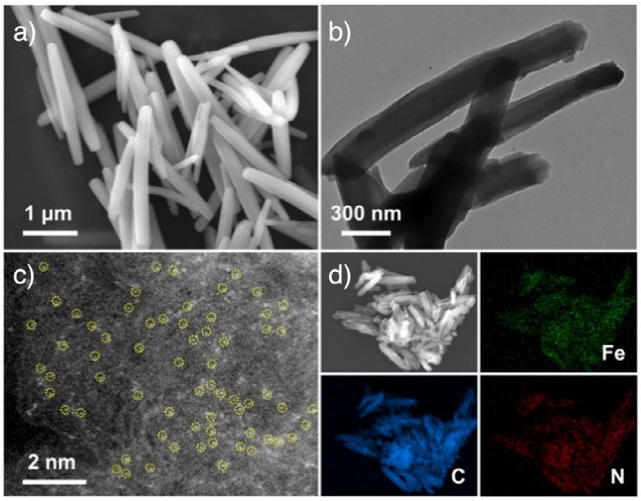

Figure 1. a) SEM image of Zn–Fe_{20}–PCN–222. b) TEM and c) HAADF-STEM images of Fe_{HL}–N–C (single-atom Fe are highlighted with yellow circles). d) EDS mapping for Fe, C, and N elements of Fe_{HL}–N–C.

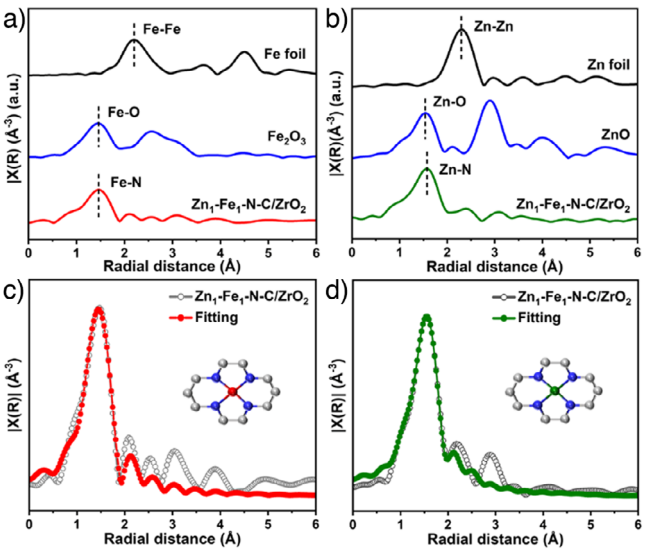

Figure 2. a) Fourier transform-extended X-ray absorption fine structure (FT-EXAFS) spectra and c) FT-EXAFS fitting results of Zn_1–Fe_1–N–C/ZrO_2 (inset: optimized coordination environment of single-atom Fe sites). b) FT-EXAFS spectra and d) FT-EXAFS fitting results of Zn_1–Fe_1–N–C/ZrO_2 (inset: optimized coordination environment of single-atom Zn sites).

mapping further illustrates the uniform distribution of Fe, N, and C species (Figure 1d). These results preliminarily indicate the successful fabrication of single-atom Fe sites within Fe_{HL}–N–C using the post-metal replacement strategy.

XAS has been adopted to further support the formation of single Fe atoms in Fe_{HL}–N–C from Zn–Fe_{20}–PCN-222. The low content of Fe-TCPP (20% of the total linkers) in the MOF effectively prevents the migration and agglomeration of Fe species during the pyrolysis, leading to the formation of single-atom Fe sites on N-doped carbon (Figure 2a). Additionally, given the low boiling point of Zn,[55] the produced Zn nanoparticles easily evaporate, leaving only single-atom Zn species, as evidenced by the absence of Zn—Zn bond in the FT-EXAFS spectrum (Figure 2b). As a result, Zn-Fe_{20}-PCN-222 is successfully converted to Zn_1-Fe_1-N-C/ZrO_2, a catalyst containing single-atom Fe (1.21 wt%) and Zn (1.05 wt%) on N-doped carbon (Figure S12a, Table S1). Further FT-EXAFS fittings reveal that both Fe and Zn atoms are isolated and coordinated with four N atoms (Figure 2c,d). Subsequently, an acid-etching process is performed to remove Zn atoms due to the fragility of the Zn–N coordination bond. Meanwhile, ZrO_2 is also eliminated during the etching process, forming Zn_v–Fe_1–N–C with abundant Zn vacancies, as confirmed by the trace amount of Zn (0.25 wt%) detected by inductively coupled plasma optical emission spectrometer (ICP-OES) (Table S1). The Fe–N coordination is more stable than Zn–N,[56] which is confirmed by the well-retained Fe loading (1.49 wt%) (Figure S12b, Table S1). The slight increase in the weight percent of Fe is likely due to the removal of ZrO_2.

The removal of single Zn atoms creates Zn vacancies with numerous dangling bonds, forming Zn_v–Fe_1–N–C materials with specific regions of relatively high energy that external metal atoms can readily refill. By leveraging this unique feature of Zn vacancies, additional Fe atoms are further introduced to fill these Zn vacancies in Zn_v–Fe_1–N–C, forming Fe_{HL}–N–C with a higher loading of Fe (2.39 wt%) (Table S1). Powder XRD pattern of Fe_{HL}–N–C shows two broad peaks corresponding to the (002) and (101) planes of carbon, without any metallic phases (Figure S13). Nitrogen sorption measurement of Fe_{HL}–N–C shows a surface area of 177.7 $m^2 \cdot g^{-1}$ with moderate pore structures (Figure S14).

To identify the chemical composition and electronic state of Fe_{HL}-N-C, X-ray photoelectron spectroscopy (XPS) analysis is performed. The N 1s XPS spectrum of Fe_{HL}-N-C demonstrates five fitted characteristic peaks corresponding to pyridinic N (397.9 eV), Fe–N_x species (398.7 eV), pyrrolic N (399.9 eV), graphitic N (400.9 eV), and oxidized N (403.1 eV) (Figure 3a).[50] The peak of Fe–N_x indicates the presence of Fe—N bonding in Fe_{HL}–N–C.

Furthermore, XAS is further utilized to provide additional insights into the electronic state and coordination structure of Fe in Fe_{HL}–N–C. In the Fe K-edge X-ray absorption near-edge structure (XANES) spectra, the energy absorption edge of Fe_{HL}–N–C, located between that of Fe foil and Fe_2O_3, signifies that Fe is in a positive charge state (Figure 3b). Notably, the FT-EXAFS spectrum of Fe_{HL}–N–C exhibits only a predominant peak at approximately 1.4 Å, attributed to the Fe–N scattering path, with no Fe–Fe peak at 2.2 Å, suggesting the exclusive formation of single-atom Fe sites (Figure 3c). Furthermore, FT-EXAFS fitting indicates that each Fe atom is coordinated with four N atoms, similar to that in Fe_{20}–N–C and Zn_v–Fe_1–N–C (Figure 3d). The results above clearly demonstrate that the post-metal replacement strategy effectively constructs single-atom Fe catalysts with improved Fe loading up to 2.39 wt%. For comparison, Fe–Fe_{20}–N–C with a Fe loading of 3.25 wt% has been further fabricated by directly modifying Fe on Fe_{20}–N–C without introducing Zn (Table S1). The absence of Zn vacancies to anchor Fe atoms results in the formation of a large number of Fe nanoparticles in Fe–Fe_{20}–N–C (Figure S15). This strongly proves that the post-metal replacement strategy, which decorates Fe with Zn

© 2025 Wiley-VCH GmbH

15213773, 2025, 27, Downloaded from https://onlinelibrary.wiley.com/doi/10.1002/anie.202501190 by University Of Science, Wiley Online Library on [13/08/2025]. See the Terms and Conditions (https://onlinelibrary.wiley.com/terms-and-conditions) on Wiley Online Library for rules of use; OA articles are governed by the applicable Creative Commons License

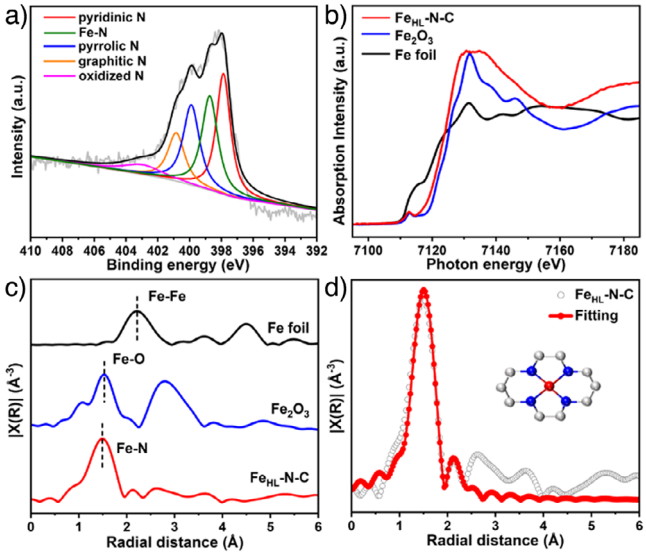

Figure 3. a) The N 1s XPS spectrum of Fe_{HL}–N–C. b) The Fe K-edge XANES and c) FT-EXAFS spectra of Fe foil, Fe_2O_3, and Fe_{HL}–N–C. d) FT-EXAFS fitting for Fe_{HL}–N–C (inset: optimized model of Fe_{HL}–N–C; the blue, gray, and red spheres represent N, C, and Fe atoms, respectively).

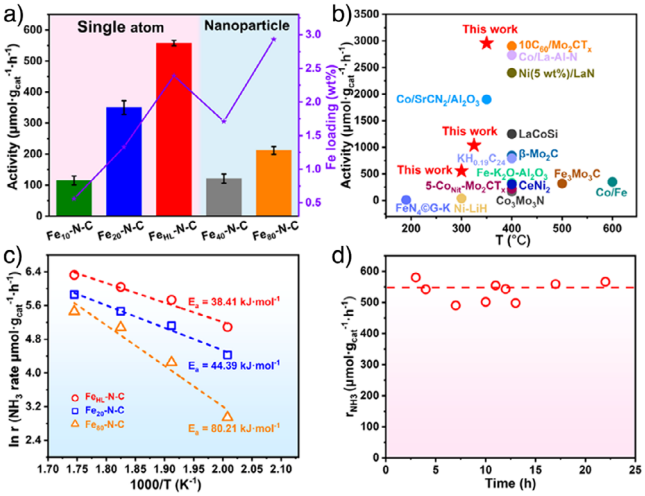

Figure 4. a) NH_3 synthesis rates over various catalysts at 300 °C and 0.1 MPa under a weight hourly space velocity (WHSV) of 30 $L{\cdot}g^{-1}_{cat}{\cdot}h^{-1}$, using a feed gas comprising 25% N_2 and 75% H_2 (Error bars represent the standard deviation based on three independent measurements). b) Performance comparison of Fe_{HL}–N–C with other reported non-precious metal catalysts for NH_3 synthesis at atmospheric pressure. c) Arrhenius plots of NH_3 synthesis for Fe_{HL}–N–C, Fe_{20}–N–C, Fe_{40}–N–C and Fe_{80}–N–C. d) Stability measurement of Fe_{HL}–N–C at 300 °C and 0.1 MPa under a WHSV of 30 $L{\cdot}g^{-1}_{cat}{\cdot}h^{-1}$.

vacancies, is an effective strategy for increasing the loading of single-atom Fe sites.

Motivated by the above results, the catalytic activities of Fe_x–N–C (x = 10, 20, 40, and 80) and Fe_{HL}–N–C catalysts for ammonia synthesis are evaluated with the assistance of the commonly used alkali metal promoter (KNa alloy).[27,57] The control experiment is performed in an empty reactor tube at 300 °C and 0.1 MPa, and no NH_3 signal is detected, excluding background NH_3 contamination or reactor-wall interactions (Figure S16). Among the series of Fe_x–N–C catalysts, the Fe_{20}–N–C presents the most optimal performance, achieving an ammonia production rate of 354 $\mu mol{\cdot}g_{cat}^{-1}{\cdot}h^{-1}$ (Figure 4a). Despite the higher metal loading, Fe_{40}–N–C and Fe_{80}–N–C exhibit inferior catalytic activity compared to Fe_{20}–N–C, highlighting the advantages of single-atom Fe sites over Fe nanoparticles (Figure 4a). Moreover, in contrast to Fe_{10}–N–C, which also contains single-atom Fe sites, Fe_{20}–N–C demonstrates enhanced catalytic performance owing to its higher Fe loading (Figure 4a). Based on the catalytic performance comparison of Fe_x–N–C samples, it can be concluded that increasing Fe loading while maintaining atomic Fe dispersion is crucial for enhancing catalytic activity.

Inspired by this, Fe_{HL}–N–C with a higher single-atom Fe loading is further adopted for NH_3 synthesis. Strikingly, Fe_{HL}–N–C exhibits exceptionally high activity up to 558 $\mu mol{\cdot}g_{cat}^{-1}{\cdot}h^{-1}$, which is even higher than that of Fe_{20}–N–C (Figure 4a). Moreover, Fe_{HL}–N–C outperforms previously reported non-precious metal catalysts that operate under ambient pressure in catalytic processes (Figure 4b). It demonstrates superior performance at lower temperature, even surpassing the industrial fused Fe catalyst and Co_3Mo_3N catalyst as well as some precious metal-based catalysts (Figure 4b, Table S2). To further demonstrate the efficacy of the post-metal replacement strategy toward enhancing catalytic activity for ammonia synthesis, the catalytic performance of the Fe–Fe_{20}–N–C catalyst, which has a slightly higher Fe loading to Fe_{HL}–N–C but contains a large number of Fe nanoparticles, is investigated. It is found that Fe–Fe_{20}–N–C presents an NH_3 synthesis activity of 347 $\mu mol{\cdot}g_{cat}^{-1}{\cdot}h^{-1}$, which is comparable to Fe_{20}–N–C yet much lower than that of Fe_{HL}–N–C (Figures S17 and S18). The catalytic performance of the Zn_v–Fe_1–N–C catalyst is also evaluated, achieving a rate of 360 $\mu mol{\cdot}g_{cat}^{-1}{\cdot}h^{-1}$ (Figures S17 and S18). Despite the presence of trace amount of Zn in Zn_v–Fe_1–N–C, its activity is similar to that of Fe_{20}–N–C, suggesting that the trace amount of Zn does not influence the catalytic performance. These results indicate that the post-metal replacement strategy provides an effective way to improve ammonia synthesis activity under mild conditions by increasing the content of single-atom Fe sites.

The apparent activation energy (E_a) for NH_3 production over Fe_{HL}–N–C and Fe_{20}–N–C, obtained from the Arrhenius plots, is empirically determined to be 38.41 and 44.39 $kJ{\cdot}mol^{-1}$, respectively (Figure 4c). However, the E_a of the iron nanoparticle catalyst Fe_{80}–N–C is 80.21 $kJ{\cdot}mol^{-1}$ (Figure 4c), much higher than those of the Fe_{20}–N–C and Fe_{HL}–N–C with single-atom Fe sites. This clearly demonstrates the superiority of single-atom Fe sites for NH_3 synthesis. Moreover, the E_a value of Fe_{HL}–N–C and Fe_{20}–N–C is substantially lower than those of representative Fe- and Ru-based catalysts (80–140 $kJ{\cdot}mol^{-1}$), indicating that the cleavage of N≡N triple bonds is no longer the rate-determining step.[58,59] In contrast, the E_a values for NH_3 production over Fe_{HL}–N–C and Fe_{20}–N–C are comparable to those of Co–N–C (~ 50 $kJ{\cdot}mol^{-1}$),[26] Ru/HZ SAC (~ 38 $kJ{\cdot}mol^{-1}$),[30] and Ru SAs/S-1 (~ 55.4 $kJ{\cdot}mol^{-1}$).[31] These researchers

© 2025 Wiley-VCH GmbH

15213773, 2025, 27, Downloaded from https://onlinelibrary.wiley.com/doi/10.1002/anie.202501190 by University Of Science, Wiley Online Library on [13/08/2025]. See the Terms and Conditions (https://onlinelibrary.wiley.com/terms-and-conditions) on Wiley Online Library for rules of use; OA articles are governed by the applicable Creative Commons License

reported that these catalysts follow an associative mechanism, where the formation of NH_x is the rate-determining step. Accordingly, an Ar temperature programmed desorption mass spectrometry (Ar-TPD-MS) analysis of the Fe_{HL}–N–C catalyst is conducted after NH_3 synthesis (Figure S19). The $*N_2H$ species, which is formed by the direct hydrogenation of N_2 without breaking the N≡N bond, is detected, clearly indicating that N_2 undergoes an associative mechanism on the single-atom Fe sites of the Fe_{HL}–N–C catalyst.

To further verify that the single-atom Fe sites are the real catalytic sites, the activity of the N–C catalyst without Fe is also tested. The result indicates that N–C shows no activity at 300 °C and 0.1 MPa, confirming the significance of single-atom Fe sites for ammonia synthesis (Table S3). Moreover, the FePc, which also features Fe–N_4 sites similar to Fe_{HL}–N–C, is tested at 300 °C and 0.1 MPa (Figure S20). It is found that the FePc presents an extremely low activity for ammonia synthesis in long-term operations. The initial NH_3 concentration likely originates from the hydrogenation of unstable nitrogen species. This further indicates that Fe–N_4 sites decorated in carbon support are much superior to iron phthalocyanine molecules. Moreover, other non-precious metal atoms have also been post-decorated into Zn_v–Fe_1–N–C to form Ni–Fe–N–C and Co–Fe–N–C (Table S4). Compared with Fe_{HL}–N–C, the Ni–Fe–N–C and Co–Fe–N–C show decreased activity (Figure S21). The discrepancy arises from their distinct N_2 adsorption capacities. According to the Sabatier principle, an optimal catalyst requires moderate adsorption capacity for reactive species. The Fe species exhibits a suitable nitrogen adsorption capacity, promoting the adsorption and subsequent activation of N_2. In contrast, the Co and Ni demonstrate comparatively weaker nitrogen adsorption capabilities, which consequently impede the adsorption and activation processes of N_2.[60–62] The results further prove the superiority of Fe sites.

Different carrier gases are fed to the isothermal reaction of Fe_{HL}–N–C to verify whether the coordinated N species in Fe_{HL}–N–C participate in ammonia synthesis. When 10% H_2/Ar without N_2 is used as the carrier gas, no ammonia signal is detected at 300 °C and 0.1 MPa (Figure S22). This indicates that ammonia does not originate from nitrogen atoms within the Fe_{HL}–N–C. To further prove this, when $^{14}N_2/H_2$ is fed into the system, only $^{14}NH_3$ is observed, whereas switching to $^{15}N_2/H_2$ results in the formation of $^{15}NH_3$ exclusively (Figure S22). These results further demonstrate that the coordinated N species do not participate in ammonia synthesis.

Also, the specific role of the alkali metal KNa alloy used in catalysis has been investigated. The N–C catalyst with KNa does not demonstrate good activity (Table S3), confirming that KNa is not a catalytic site. Furthermore, it is found that Fe_{HL}–N–C without KNa exhibits much lower activity compared to that in the presence of KNa. This suggests that, while KNa is not the catalytic site, it serves as a good promoter for Fe, significantly enhancing the activity (Table S3). A similar activity improvement is also observed for both Fe_{10}–N–C and Fe_{20}–N–C (Table S3). XPS results reveal that the introduction of KNa reduces the binding energy of Fe in Fe_{HL}–N–C (Figure S23), indicating that KNa could donate electrons to form electron-rich single-atom Fe sites. Analogous findings have also been found when KNa is introduced to Fe_x–N–C (x = 10, 20, 40, and 80) (Figures S24–S27). The activation of N_2 begins with its adsorption onto Fe sites, followed by electron transfer from Fe to the π-backbonding orbitals of N≡N.[63] The formation of electron-enriched Fe with the assistance of alkali metal promoter significantly weakens the N≡N bond, facilitating the subsequent hydrogenation processes and the formation of NH_3.[64]

In addition, the stability measurement has also been performed, revealing that Fe_{HL}–N–C maintains its excellent stability, exceeding 20 h with no significant loss in activity (Figure 4d). Additionally, the catalytic activity of the Fe_{HL}–N–C exhibits an approximately linear increase with rising pressure from 0.3 to 5 Mpa (Figure S28). The results demonstrate that hydrogen poisoning on Fe_{HL}–N–C can be avoided. During the isothermal H_2 reduction experiment of Fe_{HL}–N–C at 300 °C and 0.1 MPa (Figure S29), no discernible methane formation signal is detected, demonstrating the high stability of the carbon support under these conditions. Powder XRD and TEM characterizations for the used Fe_{HL}–N–C catalyst exhibit consistent results with those before the reaction, with no evidence of Fe agglomeration, further confirming the stability of the catalyst (Figures S30 and S31). The ammonia synthesis rate of the Fe_{HL}–N–C catalyst is also investigated at 0.1 MPa and different temperatures. The results indicate that outlet ammonia can be detected at temperatures as low as 200 °C; the ammonia production activity steadily increases along with temperature, as expected (Figure S32).

Conclusion

In summary, a post-metal replacement strategy has been developed to fabricate a single-atom Fe catalyst (Fe_{HL}–N–C) with increased Fe loading. This approach involves the synthesis of Zn–Fe–N–C with the co-decoration of single-atom Zn and Fe sites on N-doped porous carbon through the pyrolysis of a porphyrinic MOF (Zn-Fe_{20}-PCN-222). Following the substitution of single-atom Zn with Fe sites, Fe_{HL}–N–C, featuring improved Fe loading while maintaining single-atom Fe dispersion, is successfully obtained. Notably, Fe_{HL}–N–C exhibits exceptional catalytic performance toward ammonia synthesis under mild conditions. At atmospheric pressure, Fe_{HL}–N–C achieves an activity of up to 558 $\mu mol \cdot g_{cat}^{-1} \cdot h^{-1}$ for NH_3 production at 300 °C, surpassing all the lower-loading single-atom Fe catalysts (Fe_{10}–N–C and Fe_{20}–N–C), iron nanoparticle catalysts (Fe_{40}–N–C and Fe_{80}–N–C), and even traditional fused Fe catalyst and Co_3Mo_3N catalyst. Moreover, under comparable reaction conditions, the activity of Fe_{HL}–N–C exceeds that of nearly all reported non-precious metal catalysts and even some precious metal catalysts. In addition, the catalytic activity remains for over 20 h without significant decline. This work introduces an innovative approach to the preparation of single-atom catalysts with improved metal

© 2025 Wiley-VCH GmbH

15213773, 2025, 27, Downloaded from https://onlinelibrary.wiley.com/doi/10.1002/anie.202501190 by University Of Science, Wiley Online Library on [13/08/2025]. See the Terms and Conditions (https://onlinelibrary.wiley.com/terms-and-conditions) on Wiley Online Library for rules of use; OA articles are governed by the applicable Creative Commons License

loadings and establishes a foundation to explore single-atom Fe catalysts for ammonia synthesis under mild conditions.

Acknowledgements

This project was supported by the National Key Research and Development Program of China (2021YFA1500400, 2022YFA1604101), the National Natural Science Foundation of China (22331009, 22222507, W2512006), the Major Frontier Research Project of the University of Science and Technology of China (LS2060000002), and the Strategic Priority Research Program of the Chinese Academy of Sciences (XDB0450302, XDB0540000). The authors thank the 1W1B station at BSRF and 14WB1 station at SSRF for XAFS measurements. Portions of this work were conducted at the Instruments Center for Physical Science, USTC.

Conflict of Interests

The authors declare no conflict of interest.

Data Availability Statement

The data that support the findings of this study are available from the corresponding author upon reasonable request.

Keywords: Ammonia synthesis · Metal–organic frameworks · Mild conditions · MOF derivatives · Single-atom catalysts

[1] J. Kammert, J. Moon, Y. Cheng, L. Daemen, S. Irle, V. Fung, J. Liu, K. Page, X. Ma, V. Phaneuf, J. Tong, A. J. Ramirez-Cuesta, Z. Wu, *J. Am. Chem. Soc.* **2020**, *142*, 7655–7667.
[2] D. Ye, S. C. E. Tsang, *Nat. Synth.* **2023**, *2*, 612–623.
[3] L. Zhang, L. X. Ding, G. F. Chen, X. Yang, H. Wang, *Angew. Chem. Int. Ed.* **2019**, *58*, 2612–2616.
[4] F. Chang, I. Tezsevin, J. W. de Rijk, J. D. Meeldijk, J. P. Hofmann, S. Er, P. Ngene, P. E. de Jongh, *Nat. Catal.* **2022**, *5*, 222–230.
[5] Y. Sun, X. Li, Z. Wang, L. Jiang, B. Mei, W. Fan, J. Wang, J. Zhu, J.-M. Lee, *J. Am. Chem. Soc.* **2024**, *146*, 7752–7762.
[6] K. Zhang, A. Cao, L. H. Wandall, J. Vernieres, J. Kibsgaard, J. K. Nørskov, I. Chorkendorff, *Science* **2024**, *383*, 1357–1363.
[7] B. Stolz, M. Held, G. Georges, K. Boulouchos, *Nat. Energy* **2022**, *7*, 203–212.
[8] P. Wolfram, P. Kyle, X. Zhang, S. Gkantonas, S. Smith, *Nat. Energy* **2022**, *7*, 1112–1114.
[9] J. Humphreys, R. Lan, S. Tao, *Adv. Energy Sustain. Res.* **2021**, *2*, 2000043.
[10] C. Smith, A. K. Hill, L. Torrente-Murciano, *Energy Environ. Sci.* **2020**, *13*, 331–344.
[11] F.-Y. Chen, Z.-Y. Wu, S. Gupta, D. J. Rivera, S. V. Lambeets, S. Pecaut, J. Y. T. Kim, P. Zhu, Y. Z. Finfrock, D. M. Meira, G. King, G. Gao, W. Xu, D. A. Cullen, H. Zhou, Y. Han, D. E. Perea, C. L. Muhich, H. Wang, *Nat. Nanotechnol.* **2022**, *17*, 759–767.
[12] M. Ravi, J. W. Makepeace, *Chem. Sci.* **2022**, *13*, 890–908.
[13] M. Hattori, N. Okuyama, H. Kurosawa, M. Hara, *J. Am. Chem. Soc.* **2023**, *145*, 7888–7897.
[14] Y. Zhou, L. Liang, C. Wang, F. Sun, L. Zheng, H. Qi, B. Wang, X. Wang, C. Au, J. Wang, L. Jiang, H. Hosono, *J. Am. Chem. Soc.* **2024**, *146*, 23054–23066.
[15] T.-N. Ye, S.-W. Park, Y. Lu, J. Li, M. Sasase, M. Kitano, T. Tada, H. Hosono, *Nature* **2020**, *583*, 391–395.
[16] Y. Zhang, X. Peng, H. Tian, B. Yang, Z. Chen, J. Li, T. Zhang, M. Zhang, X. Liang, Z. Yu, Y. Zhou, L. Zheng, X. Wang, J. Zheng, Y. Tang, C. Au, L. Jiang, S. Xie, *Nat. Chem.* **2024**, *16*, 1781–1787.
[17] A. Sfeir, C. E. Shuck, A. Fadel, M. Marinova, H. Vezin, J. Dacquin, Y. Gogotsi, S. Royer, S. Laassiri, *J. Am. Chem. Soc.* **2024**, *146*, 20033–20044.
[18] L. Li, Y. Jiang, T. Zhang, H. Cai, Y. Zhou, B. Lin, X. Lin, Y. Zheng, L. Zheng, X. Wang, C. Xu, C. Au, L. Jiang, J. Li, *Chem* **2022**, *8*, 749–768.
[19] S. E. Sivan, K. H. Kang, S. J. Han, O. Francis Ngome Okello, S. Choi, V. Sudheeshkumar, R. W. J. Scott, H. Chae, S. Park, U. Lee, *J. Catal.* **2022**, *408*, 316–328.
[20] B. Qiao, A. Wang, X. Yang, L. F. Allard, Z. Jiang, Y. Cui, J. Liu, J. Li, T. Zhang, *Nat. Chem.* **2011**, *3*, 634–641.
[21] J. Liu, *ACS Catal.* **2017**, *7*, 34–59.
[22] L. Jiao, H.-L. Jiang, *Chem* **2019**, *5*, 786–804.
[23] W. Guo, Z. Wang, X. Wang, Y. Wu, *Adv. Mater.* **2021**, *33*, 2004287.
[24] S. K. Kaiser, Z. Chen, D. Faust Akl, S. Mitchell, J. Pérez-Ramírez, *Chem. Rev.* **2020**, *120*, 11703–11809.
[25] F. Raziq, C. Feng, M. Hu, S. Zuo, M. Z. Rahman, Y. Yan, Q.-H. Li, J. Gascon, H. Zhang, *J. Am. Chem. Soc.* **2024**, *146*, 21008–21016.
[26] X. Wang, X. Peng, W. Chen, G. Liu, A. Zheng, L. Zheng, J. Ni, C.-t. Au, L. Jiang, *Nat. Commun.* **2020**, *11*, 653–663.
[27] Z. Chen, Y. Ye, T. Peng, C. Wu, H. Li, X. Pan, X. Bao, *ACS Catal.* **2023**, *13*, 14385–14394.
[28] L. M. Azofra, N. Morlanés, A. Poater, M. K. Samantaray, B. Vidjayacoumar, K. Albahily, L. Cavallo, J.-M. Basset, *Angew. Chem. Int. Ed.* **2018**, *57*, 15812–15816.
[29] X. Li, Y. Jiao, Y. Cui, C. Dai, P. Ren, C. Song, X. Ma, *ACS Appl. Mater. Interfaces* **2021**, *13*, 52498–52507.
[30] X. Wang, L. Li, Z. Fang, Y. Zhang, J. Ni, B. Lin, L. Zheng, C.-t. Au, L. Jiang, *ACS Catal.* **2020**, *10*, 9504–9514.
[31] J.-Z. Qiu, J. Hu, J. Lan, L.-F. Wang, G. Fu, R. Xiao, B. Ge, J. Jiang, *Chem. Mater.* **2019**, *31*, 9413–9421.
[32] Y. Wang, C. Li, X. Han, J. Bai, X. Wang, L. Zheng, C. Hong, Z. Li, J. Bai, K. Leng, Y. Lin, Y. Qu, *Nat. Commun.* **2024**, *15*, 5675.
[33] Z. Zhu, H. Yin, Y. Wang, C.-H. Chuang, L. Xing, M. Dong, Y.-R. Lu, G. Casillas-Garcia, Y. Zheng, S. Chen, Y. Dou, P. Liu, Q. Cheng, H. Zhao, *Adv. Mater.* **2020**, *32*, 2004670.
[34] L. Jiao, R. Zhang, G. Wan, W. Yang, X. Wan, H. Zhou, J. Shui, S. Yu, H.-L. Jiang, *Nat. Commun.* **2020**, *11*, 2831.
[35] H. Furukawa, K. E. Cordova, M. O'Keeffe, O. M. Yaghi, *Science* **2013**, *341*, 1230444.
[36] X. Zhao, Y. Wang, D.-S. Li, X. Bu, P. Feng, *Adv. Mater.* **2018**, *30*, 1705189.
[37] P. M. Stanley, J. Haimerl, N. B. Shustova, R. A. Fischer, J. Warnan, *Nat. Chem.* **2022**, *14*, 1342–1356.
[38] S. Navalón, A. Dhakshinamoorthy, M. Álvaro, B. Ferrer, H. García, *Chem. Rev.* **2023**, *123*, 445–490.
[39] H. Li, L. Li, R.-B. Lin, W. Zhou, Z. Zhang, S. Xiang, B. Chen, *EnergyChem* **2019**, *1*, 100006.
[40] G. Li, S. Zhao, Y. Zhang, Z. Tang, *Adv. Mater.* **2018**, *30*, 1800702.
[41] A. Kirchon, L. Feng, H. F. Drake, E. A. Joseph, H. C. Zhou, *Chem. Soc. Rev.* **2018**, *47*, 8611–8638.
[42] Y.-T. Zheng, S. Li, N.-Y. Huang, X. Li, Q. Xu, *Coord. Chem. Rev.* **2024**, *510*, 215858.
[43] L. Jiao, H.-L. Jiang, *Chin. J. Catal.* **2023**, *45*, 1–5.
[44] J.-X. Peng, W. Yang, Z. Jia, L. Jiao, H.-L. Jiang, *Nano Res.* **2022**, *15*, 10063–10069.

© 2025 Wiley-VCH GmbH

15213773, 2025, 27, Downloaded from https://onlinelibrary.wiley.com/doi/10.1002/anie.202501190 by University Of Science, Wiley Online Library on [13/08/2025]. See the Terms and Conditions (https://onlinelibrary.wiley.com/terms-and-conditions) on Wiley Online Library for rules of use; OA articles are governed by the applicable Creative Commons License

[45] J. Shan, J. Liao, C. Ye, J. Dong, Y. Zheng, S.-Z. Qiao, *Angew. Chem. Int. Ed.* **2022**, *61*, e202213412.
[46] H. Huang, K. Shen, F. Chen, Y. Li, *ACS Catal.* **2020**, *10*, 6579–6586.
[47] Y. Jia, Z. Xue, J. Yang, Q. Liu, J. Xian, Y. Zhong, Y. Sun, X. Zhang, Q. Liu, D. Yao, G. Li, *Angew. Chem. Int. Ed.* **2022**, *61*, e202110838.
[48] S. Ji, Y. Chen, X. Wang, Z. Zhang, D. Wang, Y. Li, *Chem. Rev.* **2020**, *120*, 11900–11955.
[49] J. Roh, A. Cho, S. Kim, K.-S. Lee, J. Shin, J. S. Choi, J. Bak, S. Lee, J. W. Han, E. Cho, *ACS Catal.* **2023**, *13*, 9427–9441.
[50] L. Jiao, G. Wan, R. Zhang, H. Zhou, S. H. Yu, H.-L. Jiang, *Angew. Chem. Int. Ed.* **2018**, *57*, 8525–8529.
[51] M. Tong, F. Sun, Y. Xie, Y. Wang, Y. Yang, C. Tian, L. Wang, H. Fu, *Angew. Chem. Int. Ed.* **2021**, *60*, 14005–14012.
[52] Y.-Z. Chen, C. Wang, Z.-Y. Wu, Y. Xiong, Q. Xu, S.-H. Yu, H.-L. Jiang, *Adv. Mater.* **2015**, *27*, 5010–5016.
[53] W. Gao, J. Guo, P. Wang, Q. Wang, F. Chang, Q. Pei, W. Zhang, L. Liu, P. Chen, *Nat. Energy* **2018**, *3*, 1067–1075.
[54] S. Zhu, W. Yang, Y. Zhou, W. Pan, C. Wei, A. C. Y. Yuen, T. B. Y. Chen, G. H. Yeoh, H. Lu, W. Yang, *Chem. Eng. J.* **2022**, *442*, 136367.
[55] H. Liu, L. Tian, Z. Zhang, L. Wang, J. Li, X. Liang, J. Zhuang, H. Yin, D. Yang, G. Zhao, F. Su, D. W., Y. Li, *J. Am. Chem. Soc.* **2024**, *146*, 20518–20529.
[56] D. Menga, J. L. Low, Y.-S. Li, I. Arčon, B. Koyutürk, F. Wagner, F. Ruiz-Zepeda, M. Gaberšček, B. Paulus, T.-P. Fellinger, *J. Am. Chem. Soc.* **2021**, *143*, 18010–18019.
[57] R. K. Rai, W. Al Maksoud, N. Morlanés, M. Harb, R. Ahmad, A. Genovese, M. N. Hedhili, L. Cavallo, J.-M. Basset, *ACS Catal.* **2022**, *12*, 587–599.
[58] Y. Inoue, M. Kitano, M. Tokunari, T. Taniguchi, K. Ooya, H. Abe, Y. Niwa, M. Sasase, M. Hara, H. Hosono, *ACS Catal.* **2019**, *9*, 1670–1679.
[59] N. Morlanés, W. Almaksoud, R. K. Rai, S. Ould-Chikh, M. M. Ali, B. Vidjayacoumar, B. E. Al-Sabban, K. Albahily, J.-M. Basset, *Catal. Sci. Technol.* **2020**, *10*, 844–852.
[60] L. Zhang, W. Zhao, W. Zhang, J. Chen, Z. Hu, *Nano Res.* **2019**, *12*, 1181–1186.
[61] N. Zhang, Y. Gao, L. Ma, Y. Wang, L. Huang, B. Wei, Y. Xue, H. Zhu, R. Jiang, *Int. J. Hydrogen Energy* **2023**, *48*, 7621–7631.
[62] H. Yin, S.-L. Li, L.-Y. Gan, P. Wang, *J. Mater. Chem. A* **2019**, *7*, 11908–11914.
[63] Y. Baik, M. Kwen, K. Lee, S. Chi, S. Lee, K. Cho, H. Kim, M. Choi, *J. Am. Chem. Soc.* **2023**, *145*, 11364–11374.
[64] W. Al Maksoud, R. K. Rai, N. Morlanés, M. Harb, R. Ahmad, S. Ould-Chikh, D. Anjum, M. N. Hedhili, B. E. Al-Sabban, K. Albahily, L. Cavallo, J.-M. Basset, *J. Catal.* **2021**, *394*, 353–365.

Manuscript received: January 15, 2025
Revised manuscript received: April 13, 2025
Accepted manuscript online: April 23, 2025
Version of record online: May 05, 2025

© 2025 Wiley-VCH GmbH

15213773, 2025, 27, Downloaded from https://onlinelibrary.wiley.com/doi/10.1002/anie.202501190 by University Of Science, Wiley Online Library on [13/08/2025]. See the Terms and Conditions (https://onlinelibrary.wiley.com/terms-and-conditions) on Wiley Online Library for rules of use; OA articles are governed by the applicable Creative Commons License